Quantum simulation of exotic $\mathcal{PT}$-invariant topological nodal loop bands with ultracold atoms in an optical lattice

Dan-Wei Zhang,[1,2,*] Y. X. Zhao,[3,2,†] Rui-Bin Liu,[1] Zheng-Yuan Xue,[1] Shi-Liang Zhu,[4,1,5,‡] and Z. D. Wang[2,§]

[1]*Guangdong Provincial Key Laboratory of Quantum Engineering and Quantum Materials, SPTE, South China Normal University, Guangzhou 510006, China*

[2]*Department of Physics and Center of Theoretical and Computational Physics, The University of Hong Kong, Pokfulam Road, Hong Kong, China*

[3]*Max-Planck-Institute for Solid State Research, D-70569 Stuttgart, Germany*

[4]*National Laboratory of Solid State Microstructures and School of Physics, Nanjing University, Nanjing 210093, China*

[5]*Synergetic Innovation Center of Quantum Information and Quantum Physics, University of Science and Technology of China, Hefei 230026, China*

(Received 6 January 2016; published 20 April 2016)

Since the well-known $\mathcal{PT}$ symmetry has its fundamental significance and implication in physics, where $\mathcal{PT}$ denotes a joint operation of space inversion $\mathcal{P}$ and time reversal $\mathcal{T}$, it is important and intriguing to explore exotic $\mathcal{PT}$-invariant topological metals and to physically realize them. Here we develop a theory for a different type of topological metals that are described by a two-band model of $\mathcal{PT}$-invariant topological nodal loop states in a three-dimensional Brillouin zone, with the topological stability being revealed through the $\mathcal{PT}$-symmetry-protected nontrivial $\mathbb{Z}_2$ topological charge even in the absence of both $\mathcal{P}$ and $\mathcal{T}$ symmetries. Moreover, the gapless boundary modes are demonstrated to originate from the nontrivial topological charge of the bulk nodal loop. Based on these exact results, we propose an experimental scheme to realize and to detect tunable $\mathcal{PT}$-invariant topological nodal loop states with ultracold atoms in an optical lattice, in which atoms with two hyperfine spin states are loaded in a spin-dependent three-dimensional optical lattice and two pairs of Raman lasers are used to create out-of-plane spin-flip hopping with site-dependent phase. It is shown that such a realistic cold-atom setup can yield topological nodal loop states, having a tunable band-touching ring with the twofold degeneracy in the bulk spectrum and nontrivial surface states. The nodal loop states are actually protected by the combined $\mathcal{PT}$ symmetry and are characterized by a $\mathbb{Z}_2$-type invariant (or topological charge), i.e., a quantized Berry phase. Remarkably, we demonstrate with numerical simulations that (i) the characteristic nodal ring can be detected by measuring the atomic transfer fractions in a Bloch-Zener oscillation; (ii) the topological invariant may be measured based on the time-of-flight imaging; and (iii) the surface states may be probed through Bragg spectroscopy. The present proposal for realizing topological nodal loop states in cold-atom systems may provide a unique experimental platform for exploring exotic $\mathcal{PT}$-invariant topological physics.

DOI: 10.1103/PhysRevA.93.043617

I. INTRODUCTION

Since the discovery of topological insulators, the study of band topology of insulating and semimetallic materials has attracted a broad interest [1–16]. Significant theoretical progress has been made in the classification of various kinds of gapped and gapless topological band systems [3–11]. Very recently, with regard to exploring symmetry-protected topological phases, attention seems to have shifted from gapped insulators or superconductors to gapless metals or semimetals. For three-dimensional systems, two kinds of topological semimetals, consisting, respectively, of the nodal point and the nodal loop (NL), have been addressed [17–22]. Weyl semimetals [18–20] and certain Dirac semimetals [9,17] belong to the former, which have twofold- and fourfold-degenerate Fermi points, respectively, and which are topologically protected by a topological invariant (such as the Chern number for Weyl semimetals) and give rise to exotic Fermi-arc surface states [17–20]. NL semimetal, in contrast, has the valence and conduction bands crossing along closed lines instead of isolated points, which may topologically be protected by certain discrete symmetry and may give rise to nearly flat surface bands [21,22]. Weyl and Dirac semimetals have been theoretically and experimentally explored not only in materials [9,17–20,23–28] but also in some artificial systems, such as photonic and acoustic crystals [29–31]. However, topological NL bands have yet to be experimentally observed or realized, even though some theoretical proposals were suggested for their realization in real materials very recently [32–37]. In addition, the so-called $\mathcal{PT}$ symmetry may actually be understood as a generalized inversion symmetry with regard to the space-time dimension, which is fundamental in physics, and thus a realistic model for describing exotic $\mathcal{PT}$-invariant topological NLs is highly desirable. Notably, a purely combined $\mathcal{PT}$-invariant topological NL state that has neither $\mathcal{P}$ nor $\mathcal{T}$ symmetry can hardly be realized in real condensed materials, and thus its physical implementation presents a great challenge to physicists both theoretically and experimentally.

On the other hand, fortunately, ultracold atoms in optical lattices [38] with a synthetic electromagnetic field and spin-orbit coupling [13–15] provide a clean and tunable platform

*zdanwei@126.com
†yuxinphy@hku.hk
‡slzhu@nju.edu.cn
§zwang@hku.hk

for exploring exotic topological quantum phases [39–46]. Remarkably, the Zak phase in topologically nontrivial Bloch bands realized in one-dimensional double-well optical lattices has been measured [39]. By engineering the atomic hopping configurations in optical lattices, the celebrated Harper-Hofstadter [47] and Haldane models [48] have been realized [40–43], where the Chern number characterizing the topological bands has also been measured. The experimental observation of chiral edge states in one-dimensional optical lattices subjected to a synthetic magnetic field and an artificial dimension has also been reported [45,46]. An important question then is whether the other predicted topological phases that are rare in solid-state materials can be realized in these cold-atom systems. Several schemes have been proposed to realize $\mathbb{Z}_2$ topological insulators [49,50], chiral topological states [51–53], and topological nodal point semimetals [54–59] using ultracold atoms in optical lattices. However, an experimentally feasible and tunable scheme for realizing the combined $\mathcal{PT}$ topological NL states and their detection is still badly needed.

In this article, we first depict the classification of topological NLs in systems with pure $\mathcal{PT}$ symmetry. In three-dimensional momentum space, only $\mathcal{PT}$-invariant NLs are topologically protected with a $\mathbb{Z}_2$ charge. We then construct a theoretical model to realize the topologically nontrivial NL, and we demonstrate its topological stability under $\mathcal{PT}$-invariant perturbations that break both $\mathcal{T}$ and $\mathcal{P}$ symmetries. It is also shown that the nontrivial topological charge of the bulk NL directly determines the certain boundary gapless modes. Based on these theoretical results, we propose an experimental scheme to realize and to detect tunable $\mathcal{PT}$-invariant topological NL states with ultracold atoms in an optical lattice. In our proposal, fermionic (or bosonic) atoms with two hyperfine spin states are loaded in a spin-dependent three-dimensional optical lattice, and two pairs of Raman lasers are used to create out-of-plane spin-flip hopping with site-dependent phase. We show that such a realistic cold-atom setup can yield topological NL states having tunable ring-shaped band-touching lines with twofold degeneracy in the bulk spectrum and nontrivial surface states. The NL states are actually topologically protected by the combined $\mathcal{PT}$ symmetry even in the presence of $\mathcal{P}$- and $\mathcal{T}$-breaking perturbations, and they are characterized by a quantized Berry phase (a $\mathbb{Z}_2$-type invariant). Moreover, with numerical simulations, we demonstrate that (i) the characteristic nodal ring can be detected by measuring the atomic transfer fractions in a Bloch-Zener oscillation; (ii) the topological invariant (charge) can be measured based on the time-of-flight imaging; and (iii) the surface states may be probed through Bragg spectroscopy. The realization of the combined $\mathcal{PT}$ topological NL states in cold-atom systems would definitely be of great importance in contributing to topological matter research across disciplines.

The paper is organized as follows. Section II describes the topological classification of NLs in systems with combined $\mathcal{PT}$ symmetry, it interprets the physical meanings of the $\mathbb{Z}_2$ topological invariant in a lattice model, and it discusses the topological stability against perturbations preserving $\mathcal{PT}$ symmetry but breaking both $\mathcal{P}$ and $\mathcal{T}$ symmetries. In Sec. III, we propose an experimentally feasible scheme for realizing the $\mathcal{PT}$-invariant topological NL states with ultracold atoms in an optical lattice. We first introduce the proposed system and lattice model, and then we study the tunable NLs and their experimental detection. In Sec. IV, we elaborate on the topological properties of the simulated NL states by calculating the quantized Berry phase and the surface states, and we also present practical methods for their experimental detection in the cold-atom system with numerical simulations. Finally, a short conclusion is given in Sec. V.

II. CLASSIFICATION OF $\mathcal{PT}$-INVARIANT TOPOLOGICAL METALS OR SEMIMETALS AND THE TOPOLOGICAL STABILITY OF NODAL LOOPS

In this section, we first describe a mathematically rigorous classification of topological metals or semimetals protected by $\mathcal{PT}$ symmetry using the KO theory. Then we construct a physically realistic $\mathcal{PT}$-invariant NL model, which has a nontrivial $\mathbb{Z}_2$ topological charge. The stability of the NL is investigated in detail, making concrete implications of its nontrivial topological charge. Other physical meanings of the topological charge are also discussed.

A. Classification of topological metals or semimetals with $\mathcal{PT}$ symmetry

Let us consider a noninteracting fermionic system, which is described by the Hamiltonian $\mathcal{H}(k)$ in momentum space. For such a system, the time-reversal $\mathcal{T}$ and inversion $\mathcal{P}$ symmetries are represented by $\hat{T}$ and $\hat{P}$ as, respectively,

$$\hat{T}\mathcal{H}(k)\hat{T}^{-1} = \mathcal{H}(-k), \quad \hat{P}\mathcal{H}(k)\hat{P}^{-1} = \mathcal{H}(-k). \tag{1}$$

$\hat{T}$ is antiunitary while $\hat{P}$ is unitary,

$$\hat{T}i\hat{T}^{-1} = -i, \quad \hat{P}i\hat{P}^{-1} = i. \tag{2}$$

We are interested here mainly in the combined symmetry $\mathcal{A} = \mathcal{PT}$, namely only $\mathcal{PT}$ is required to be preserved, while $\mathcal{T}$ and $\mathcal{P}$ may be broken individually. The operation of the antiunitary symmetry $\mathcal{A}$ is given by

$$\hat{A}\mathcal{H}(k)\hat{A}^{-1} = \mathcal{H}(k), \quad \hat{A}i\hat{A}^{-1} = -i. \tag{3}$$

It is clear that $\mathcal{A}$ operates in a pointwise fashion in momentum space as an antiunitary operator, and therefore the corresponding Berry bundle generated by $\mathcal{H}(k)$ in the gapped region has a real relation on each fiber, since every state $|\alpha,k\rangle$ and its complex conjugate $|\alpha,k\rangle^*$ are related by a unitary transformation, namely $U_A|\alpha,k\rangle^* = |\alpha,k\rangle$. The topological classification of fiber bundles with such a pointwise real relation (and a high enough dimension) is given by an Abelian group in the framework of the KO theory, where each group element corresponds to a topological class [60]. The Clifford algebra may be used as a powerful tool in the computation of the KO groups [61], as illustrated below [62].

To find the topological space of the gapped Hamiltonians under the restriction of the symmetry $\mathcal{A}$, we recombine the relevant operators as $\hat{A}$, $i\hat{A}$, and $i\mathcal{H}$, which anticommute with each other forming a Clifford algebra,

$$\{\hat{A}, i\hat{A}\} = 0, \quad \{\hat{A}, i\mathcal{H}\} = 0, \quad \{i\mathcal{H}, i\hat{A}\} = 0. \tag{4}$$

For any gapped k, we adiabatically flatten $\mathcal{H}(k)$ to be $\tilde{\mathcal{H}}(k)$, which has the unital normalization $\tilde{\mathcal{H}}^2(k) = 1_N$, with 1_N being

the $N \times N$ identity matrix. It is sufficient, for topological purposes, to consider $\tilde{\mathcal{H}}$. Thus for the gapped region of momentum space, we assume, without loss of generality, the following normalizations:

$$(i\mathcal{H})^2 = -1, \quad \hat{A}^2 = (i\hat{A})^2 = \pm 1, \tag{5}$$

where $\hat{A}^2 = (i\hat{A})^2$ comes from the antiunitarity of $\hat{A}$ in Eq. (3).

For the case of $\hat{A}^2 = 1$, it is found that $\hat{A}$ and $i\hat{A}$ form the Clifford algebra $C^{0,2}$, which is extended by the $i\mathcal{H}$ to be $C^{1,2}$. Since $C^{0,2} \subset C^{1,2} \approx C^{0,0} \subset C^{0,1}$ [60,61], it is found that the space of the gapped Hamiltonians $\mathcal{H}(k)$ is given by the classifying space R_0 up to homotopy. For an NL in three-dimensional momentum space, we may choose a circle S^1 to enclose the NL from its gapped transverse dimensions, and $\mathcal{H}|_{S^1}(k)$ gives a map from S^1 to R_0, which is classified by the KO theory as [60,61]

$$\widetilde{KO}(S^1) \cong \pi_1(R_0) \cong \pi_0(R_1) \cong \mathbb{Z}_2. \tag{6}$$

This result implies that there exists a topological nontrivial class of NLs with $\mathbb{Z}_2$ charge, whose topological stability depends solely on the combined $\mathcal{TP}$ symmetry, regardless of individual $\mathcal{T}$ and $\mathcal{P}$ symmetries.

B. A two-band nodal loop model and the meanings of its topological charge

We now construct a simple two-band model, which has $\mathcal{PT}$ symmetry with $(\hat{P}\hat{T})^2 = 1$, to illustrate our theory. A two-band model may be written in a unified form $\mathcal{H}(k) = f_\mu(k)\sigma^\mu$, where f_μ are real functions of k and $\sigma^\mu = (\sigma_0, \sigma_j)$ are Pauli matrices. Choosing the time-reversal and inversion symmetry as $\hat{T} = \mathcal{K}$, with $\mathcal{K}$ as the complex-conjugate operator and $\hat{P} = \sigma_3$, the $\mathcal{PT}$ symmetry with $\hat{A} = \sigma_3\mathcal{K}$ requires

$$\sigma_3\mathcal{H}^*(k)\sigma_3 = \mathcal{H}(k), \tag{7}$$

which simply means the absence of the σ_1 term in $\mathcal{H}(k)$. The time-reversal symmetry implies

$$\mathcal{H}^*(k) = \mathcal{H}(-k), \tag{8}$$

leading to the fact that the coefficients of σ_0, σ_1, and σ_3 are even functions of k, while that of σ_2 is odd. Note that the conservation of $\mathcal{TP}$ and $\mathcal{T}$ implies also the conservation of $\mathcal{P}$. From the above points, we start with a simple continuum model in three dimensions as

$$\mathcal{H}_0(\mathbf{k}) = [R^2 - B(k_x^2 + k_y^2) - B_z k_z^2]\sigma_3 + C_z k_z \sigma_2 \tag{9}$$

with $\mathbf{k} = (k_x, k_y, k_z)$ and $B > 0$, which has both $\mathcal{P}$ and $\mathcal{T}$ symmetries, and therefore $\mathcal{PT}$ symmetry. Note that we abandon the σ_0 term for clarity, since it has nothing to do with the spectrum gap. We also keep the rotation symmetry of the k_x-k_y plane for simplicity. It is found that the gapless points form an NL on the k_x-k_y plane with $k_z = 0$, which may be enclosed by a loop from the gapped region, for instance a tiny circle on the k_y-k_z plane as shown in Fig. 1. The circle is parametrized as $(0, R/\sqrt{B} + \rho\cos\phi, \rho\sin\phi)$, where ρ is the radius and ϕ is the angle. If ρ is sufficiently small, the Hamiltonian restricted on the circle is expanded as

$$h(\phi) = -2\sqrt{B}R\rho\cos\phi\sigma_3 + C_z\rho\sin\phi\sigma_2 + O(\rho^2). \tag{10}$$

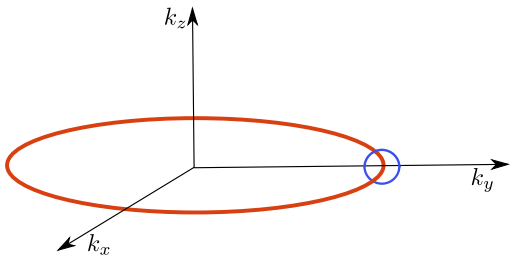

FIG. 1. An NL in three-dimensional momentum space, enclosed by a tiny circle.

It is a well-known result that the Berry phase of the occupied state wave function of such a Hamiltonian is equivalent to 1 modulo 2, namely

$$\gamma_{S^1} = \frac{1}{\pi}\int a(\phi)d\phi \equiv 1 \mod 2, \tag{11}$$

where $a(\phi) = \langle\phi|i\partial_\phi|\phi\rangle$ with $|\phi\rangle$ being the occupied state of $h(\phi)$. The unit topological charge γ means the NL is in the nontrivial class of the $\mathbb{Z}_2$ classification, which was obtained above.

According to our classification theory, the topological protection of the stability of the gapless modes requires only combined $\mathcal{PT}$ symmetry, rather than both $\mathcal{P}$ and $\mathcal{T}$ symmetries. In other words, the gapless modes still exist for topological reasons under perturbations breaking both $\mathcal{P}$ and $\mathcal{T}$ symmetries but preserving $\mathcal{PT}$ symmetry. In general, a σ_2 term with even functions of $\mathbf{k}$ and a σ_3 term with odd functions of $\mathbf{k}$ break both $\mathcal{P}$ and $\mathcal{T}$. From our discussion of $\mathcal{P}$ and $\mathcal{T}$ symmetries above, the perturbations below, for instance, satisfy the symmetry conditions

$$\mathcal{H}'(\mathbf{k}) = [D(k_x + k_y) + D_z k_z]\sigma_3 + \left[\mu + \epsilon_z k_z^2 + \epsilon\left(k_x^2 + k_y^2\right)\right]\sigma_2, \tag{12}$$

under which gapless modes still survive, although the shape of the NL has been distorted. For instance, when ϵ and ϵ_z vanish, the gapless region is given by the solution of the equation

$$B\left(k_x^2 + k_y^2\right) - D(k_x + k_y) + \left[B_z(\mu/C_z)^2 + D_z\mu/C_z - \kappa^2\right] = 0, \tag{13}$$

for which it is seen that the radius of the NL is changed and the center is moved by the perturbations.

We now consider the realistic situation that the NL exists in a lattice model, where the momentum coordinates are periodic, forming a Brillouin zone as illustrated in Fig. 2. The NL in Fig. 2 as the collection of gapless points is still denoted by the red circle as in Fig. 1. But in a lattice model the periodicity of the momentum coordinates allows large circles, such as L_1 and L_2 in Fig. 1, since the two ends of such a line segment are identified. Thus for a lattice model, the tiny circle in Fig. 1 enclosing the NL can be continuously deformed to be the S^1 in the gapped region, which may further be divided as two large circles L_1 and L_2, namely

$$S^1 \approx L_1 - L_2 \tag{14}$$

with the sign indicating the direction of the line. The topological charges satisfy the relation

$$\gamma_{S^1} = \gamma_{L_1} - \gamma_{L_2} \mod 2, \tag{15}$$

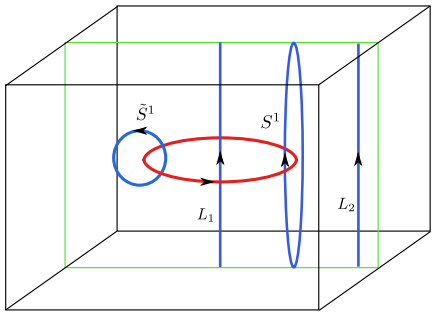

FIG. 2. An NL in a three-dimensional Brillouin zone, enclosed by different loops.

where actually L_1 and L_2 can be any large circles inside and outside the NL, respectively, as in Fig. 2. For a topologically nontrivial NL, if the topological charge of any outside line is trivial, then every large circle going inside the NL has nontrivial topological charge. For straight lines inside, each of them may be regarded as corresponding to a one-dimensional gapped system that is of a topologically nontrivial band structure, leading to certain gapless boundary modes.

The arguments above are applicable to general cases in the classification. We may note an essential difference between $\mathbb{Z}$ and $\mathbb{Z}_2$ topological charges, namely for $\mathbb{Z}$ topological charge, reversing the direction also reverses the topological charge, while $\mathbb{Z}_2$ topological charge is insensitive to the direction since $1 \equiv -1 \mod 2$ [12].

III. $\mathcal{PT}$-INVARIANT NODAL LOOP STATES IN COLD-ATOM SYSTEMS

Although the two-band Hamiltonian of $\mathcal{PT}$-invariant NL is simple, the direct implementation of this ideal model in electronic materials is difficult due to the spin-orbit coupling or complex lattice structure therein [32–37]. In this section, we propose an experimental scheme to realize and detect tunable $\mathcal{PT}$-invariant topological NL states with ultracold atoms in a three-dimensional optical lattice. We first describe the proposed system and the lattice model, which may have both $\mathcal{P}$ and $\mathcal{T}$ symmetries or generically only preserves the combined $\mathcal{PT}$ symmetry while breaking both of them. Then we study the tunable NLs and their experimental detection in this cold-atom system.

A. Proposed cold-atom system and lattice model

Our proposed system is based on a fermionic gas (or bosonic gas) of noninteracting atoms with two chosen hyperfine spin states $|\uparrow\rangle$ and $|\downarrow\rangle$ in a spin-dependent cubic optical lattice, as shown in Fig. 3(a). The lattice potential takes the form

$$V_\sigma(\mathbf{r}) = -V_{0,\sigma}[\cos^2(k_0 x) + \cos^2(k_0 y) + \cos^2(k_0 z)], \quad (16)$$

where $\sigma = \uparrow, \downarrow$, $V_{0,\sigma}$ denote the potential strengths for the spin state $|\sigma\rangle$, and k_0 is the wave number with the lattice constant $a = \pi/k_0$. As shown in Fig. 3(a), we consider a two-photon Raman transition between $|\uparrow\rangle$ and $|\downarrow\rangle$ along the z axis, which is achieved by coupling the two ground hyperfine states to an excited state $|e\rangle$ with a large single-photon detuning Δ_d. In addition, the two hyperfine states differ in the magnetic

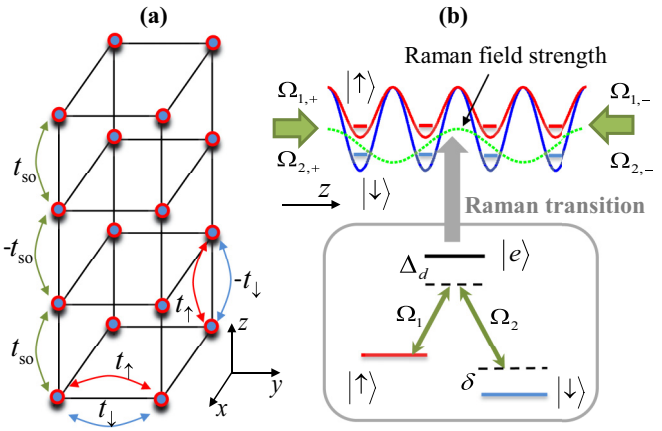

FIG. 3. The proposed cold-atom system and laser configuration. (a) The cubic optical lattice and the effective atomic hopping configuration between nearest-neighbor lattice sites. It contains the spin-conserved hopping $t_\uparrow$ along each axis, $t_\downarrow$ in the xy plane but $-t_\downarrow$ out of the plane, the spin-flip hopping from $|\downarrow\rangle$ to $|\uparrow\rangle$, which is $\pm t_{so}$ staggered along the z axis, and its Hermitian conjugation progress. (b) The spin-dependent lattice structure and laser configuration of the Raman transition between spin states $|\uparrow\rangle$ and $|\downarrow\rangle$ along the z axis. The effective Raman field strength proportional to $\sin(k_0 z)$ (green dotted line) consists of two pairs of plane waves denoted by their Rabi frequencies $\Omega_{1,\pm}$ (which gives the laser field Ω_1) and $\Omega_{2,\pm}$ (which gives the laser field Ω_2). Two spin states are coupled via a two-photon Raman transition with a large detuning Δ_d from an excited state $|e\rangle$ and a two-photon detuning δ.

quantum number by 1 and thus the atomic addressing is achieved through polarization selection. This configuration has been used to create the equal-Rashba-Dresselhaus spin-orbit interaction [13–15]. The Rabi frequencies of the corresponding laser fields are chosen as $\Omega_1(z) = \Omega_0 \cos(k_0 z/2) e^{ik_0' z}$ and $\Omega_2(z) = \Omega_0 \sin(k_0 z/2)$, respectively, where Ω_0 is the strength constant controlled by the laser intensities of the Raman fields and k_0' denotes a small deviation of the wave numbers ($k_0' \ll k_0$) that can be tuned from zero to finite value via the laser beams. Here Ω_1 and Ω_2 can be realized, respectively, with a pair of laser beams $\Omega_{1,\pm} = \frac{1}{2}\Omega_0 e^{\pm i(k_0 \pm k_0')z}$ and $\Omega_{2,\pm} = \frac{1}{2}\Omega_0 e^{\pm i(k_0 z + \pi/2)}$. Generally, there is a two-photon detuning δ in the Raman transition, as shown in Fig. 3(b).

In the presence of large detuning $|\Delta| \gg \Omega_0, |\delta|$ for the Raman transition, we can eliminate the excited state and consider the atomic motions in the ground-state manifold. Under this condition, the effective single-particle Hamiltonian in the spin basis $\{|\uparrow\rangle, |\downarrow\rangle\}$ is given by

$$H_0 = \frac{\mathbf{p}^2}{2m_a} + \begin{pmatrix} V_\uparrow(\mathbf{r}) & \hbar\Omega_{\text{eff}}(z) \\ \hbar\Omega_{\text{eff}}^*(z) & V_\downarrow(\mathbf{r}) + \hbar\delta \end{pmatrix}, \quad (17)$$

where $\mathbf{p}$ and m_a, respectively, denote the atomic momentum and mass, and $\Omega_{\text{eff}}(z) = \frac{\Omega_1^* \Omega_2}{\Delta_d} = \frac{\Omega_0^2 e^{-ik_0' z}}{2\Delta_d} \sin(k_0 z)$ denotes the resulting Raman coupling in the two-photon transition. We consider all the atoms in the lowest band of the optical lattice, and then the Hamiltonian in the second quantization formalism takes the form

$$\hat{H} = \int d^3\mathbf{r}' \Psi^\dagger(\mathbf{r}') H_0 \Psi(\mathbf{r}'). \quad (18)$$

Here $\Psi = (\Psi_\uparrow, \Psi_\downarrow)^{\mathrm{T}}$ is the two-component field operator with $\Psi_\sigma(\mathbf{r}') = \sum_{\mathbf{r}} \hat{a}_{\mathbf{r},\sigma} w_\sigma(\mathbf{r}' - \mathbf{r})$, which is expanded in terms of the Wannier function $w_\sigma(\mathbf{r}' - \mathbf{r})$ and $\hat{a}_{\mathbf{r},\sigma}$ representing the annihilation operator of the fermionic mode of the spin state $|\sigma\rangle$ at the lattice site $\mathbf{r}$. A straightforward calculation yields the tight-binding Hamiltonian

$$\begin{aligned}\hat{H} = &-\sum_{\mathbf{r},\sigma,\eta} t_\sigma \hat{a}^\dagger_{\mathbf{r},\sigma} \hat{a}_{\mathbf{r}+\hat{\eta},\sigma} + \mathrm{H.c.} \\ &+ \sum_{\mathbf{r},\pm} t_s^{\mathbf{r},\mathbf{r}\pm\hat{\mathbf{z}}} \hat{a}^\dagger_{\mathbf{r},\uparrow} \hat{a}_{\mathbf{r}\pm\hat{\mathbf{z}},\downarrow} + \mathrm{H.c.} \\ &+ \sum_{\mathbf{r}} m_z (\hat{a}^\dagger_{\mathbf{r},\uparrow} \hat{a}_{\mathbf{r},\uparrow} - \hat{a}^\dagger_{\mathbf{r},\downarrow} \hat{a}_{\mathbf{r},\downarrow}). \end{aligned} \tag{19}$$

Here the spin-conserved hopping along the η axis ($\eta = x, y, z$) is derived as $t_\sigma = -\int d^3\mathbf{r}' w^*_\sigma(\mathbf{r}' - \mathbf{r})[\frac{\mathbf{p}^2}{2m_a} + V_\sigma] w_\sigma(\mathbf{r}' - \mathbf{r} - \hat{\eta}) \approx (4/\sqrt{\pi}) V_{0,\sigma}^{3/4} E_R^{1/4} e^{-2\sqrt{V_{0,\sigma}/E_R}}$ in the harmonic approximation (by using Gaussian wave functions of the ground state centered in each lattice well for the Wannier functions), with $E_R = \hbar^2 k_0^2 / 2m_a$ being the recoil energy [63]. The spin-flip hopping terms induced by the Raman field take the form $t_s^{\mathbf{r},\mathbf{r}\pm\hat{\mathbf{z}}} = \int d^3\mathbf{r}' w^*_\uparrow(\mathbf{r}' - \mathbf{r}) \hbar\Omega_{\mathrm{eff}}(\mathbf{r}') w_\downarrow(\mathbf{r}' - \mathbf{r} \mp \hat{\mathbf{z}})$.

In this lattice system, the strength of the Raman field proportional to $\sin(k_0 z)$ and the lowest band Wannier functions are antisymmetric and symmetric with respect to the center of each lattice site, respectively. Due to this spatial configuration, the periodic field does not couple the intrasite spins, and the spin-flip hopping terms satisfy $t_s^{\mathbf{r},\mathbf{r}\pm\hat{\mathbf{z}}} = \pm(-1)^{z/a} e^{\pm i\varphi} t_{\mathrm{so}}$ [51], where $t_{\mathrm{so}} = \frac{\hbar\Omega_0^2}{2\Delta_d} \int dx\, w^*_\uparrow(x) w_\downarrow(x) \int dy\, w^*_\uparrow(y) w_\downarrow(y) \int dz\, w^*_\uparrow(z) e^{ik_0' z} \sin(k_0 z) w_\downarrow(z - a)$ and $\varphi = k_0' a$. The last term $m_z = (V_{0,\uparrow} - V_{0,\downarrow} - \hbar\delta)/2$ is equivalent to a Zeeman field along the z axis and can be precisely tuned via the laser frequencies of the Raman beams with an acoustic-optic modulator or through the lattice potentials for fixed laser frequencies. By redefining the spin-down operator $\hat{a}_{\mathbf{r},\downarrow} \to e^{i\pi z/a} \hat{a}_{\mathbf{r},\downarrow}$, Hamiltonian (19) can be rewritten as

$$\begin{aligned}\hat{H} = &-\sum_{\mathbf{r},\sigma} t_\sigma (\hat{a}^\dagger_{\mathbf{r},\sigma} \hat{a}_{\mathbf{r}+\hat{\mathbf{x}},\sigma} + \hat{a}^\dagger_{\mathbf{r},\sigma} \hat{a}_{\mathbf{r}+\hat{\mathbf{y}},\sigma}) + \mathrm{H.c.} \\ &- \sum_{\mathbf{r}} (t_\uparrow \hat{a}^\dagger_{\mathbf{r},\uparrow} \hat{a}_{\mathbf{r}+\hat{\mathbf{z}},\uparrow} - t_\downarrow \hat{a}^\dagger_{\mathbf{r},\downarrow} \hat{a}_{\mathbf{r}+\hat{\mathbf{z}},\downarrow}) + \mathrm{H.c.} \\ &+ \sum_{\mathbf{r}} t_{\mathrm{so}} (e^{i\varphi} \hat{a}^\dagger_{\mathbf{r},\uparrow} \hat{a}_{\mathbf{r}+\hat{\mathbf{z}},\downarrow} - e^{-i\varphi} \hat{a}^\dagger_{\mathbf{r},\uparrow} \hat{a}_{\mathbf{r}-\hat{\mathbf{z}},\downarrow}) + \mathrm{H.c.} \\ &+ \sum_{\mathbf{r}} m_z (\hat{a}^\dagger_{\mathbf{r},\uparrow} \hat{a}_{\mathbf{r},\uparrow} - \hat{a}^\dagger_{\mathbf{r},\downarrow} \hat{a}_{\mathbf{r},\downarrow}). \end{aligned} \tag{20}$$

Figure 3(a) also shows this effective atomic hopping configuration for the $\varphi = 0$ (i.e., $k_0' = 0$) case in the optical lattice.

In the three-dimensional Brillouin zone, the resultant Bloch Hamiltonian is given by

$$\mathcal{H}_B = f_z(\mathbf{k})\sigma_3 - 2t_{\mathrm{so}} \sin(k_z a + \varphi)\sigma_2 - f_0(\mathbf{k})\sigma_0, \tag{21}$$

where $f_z(\mathbf{k}) = m_z - \alpha_-[\cos(k_x a) + \cos(k_y a)] - \alpha_+ \cos(k_z a)$ and $f_0(\mathbf{k}) = \alpha_+[\cos(k_x a) + \cos(k_y a)] + \alpha_- \cos(k_z a)$, where $\alpha_\pm \equiv t_\uparrow \pm t_\downarrow$ are also tunable parameters. The Bloch Hamiltonian can be rewritten as

$$\mathcal{H}_B = \tilde{\mathcal{H}}_0 + \mathcal{H}_P, \tag{22}$$

where $\tilde{\mathcal{H}}_0 = f_z(\mathbf{k})\sigma_3 - 2t_{\mathrm{so}} \cos\varphi \sin(k_z a)\sigma_2 - f_0(\mathbf{k})\sigma_0$ and the perturbation part $\mathcal{H}_P = -2t_{\mathrm{so}} \sin\varphi \cos(k_z a)\sigma_2$. Here $\tilde{\mathcal{H}}_0$ preserves both $\mathcal{P}$ and $\mathcal{T}$ symmetries but $\mathcal{H}_P$ (which vanishes in the case $\varphi = 0$) breaks the two symmetries. However, the whole Hamiltonian $\mathcal{H}_B$ satisfies the combined $\mathcal{PT}$ symmetry. As analyzed in Sec. II, this guarantees the existence and topological stability of symmetry-protected NLs in the three-dimensional Brillouin zone. The perturbation part $\mathcal{H}_P$ in this system only shifts the center of the NLs by replacing $k_z a \to k_z a + \varphi$, and it does not modify their shape and topological properties. Therefore, without loss of generality, we take the $\varphi = 0$ case in the following sections to study the NL states and their detection in this system. Note that the proposed optical lattice system and the Raman coupling scheme are also applicable to the bosonic atoms [13–15,40–42]. As for other different types of NL states, a four-band model allowing Dirac or Weyl rings was also recently suggested to be simulated with cold atoms [64].

B. Tunable nodal loop states

Now we proceed to study the properties and the detection method of the NL states in the proposed model system. For $\varphi = 0$, the bulk spectrum is $E_\pm(\mathbf{k}) = f_0(\mathbf{k}) \pm \sqrt{4t_{\mathrm{so}}^2 \sin^2(k_z a) + f_z(\mathbf{k})^2}$. The bulk bands are fully gapped except for the points in momentum positions that satisfy the following conditions:

$$\cos(k_x a) + \cos(k_y a) = (m_z - \alpha_+)/\alpha_- \mathrm{for} k_z = 0, \tag{23}$$

$$\cos(k_x a) + \cos(k_y a) = (m_z + \alpha_+)/\alpha_- \mathrm{for} k_z = \pi/a, \tag{24}$$

which can give rise to NLs with twofold degeneracy in the three-dimensional Brillouin zone. Without loss of generality, we assume $t_\uparrow \geqslant t_\downarrow > 0$. Since the effective Zeeman field and the hopping amplitudes can be tuned independently, we can define two ratio parameters $\beta = m_z/\alpha_-$ and $\tau = \alpha_+/\alpha_-$ in this system.

We then numerically solve Eqs. (23) and (24) for the existence and the shape of the NLs, and the resultant phase diagram is shown in Fig. 4(a), where the phases III, II.a, II.b, and I, respectively, correspond to a trivial insulator, an NL on the $k_z = 0$ plane, an NL on the $k_z = \pi/a$ plane, and two coexisting NLs on the two planes. The two NLs belong to the same nontrivial $\mathbb{Z}_2$ case as that discussed in the preceding section. During the increase of β (denoted by the black solid arrows in Fig. 4), the NLs have the same evolution procession as illustrated in Fig. 4(b). First, a singular point is created at the corner of the sub-Brillouin zone with $k_z = 0$ or π/a, and then it is spread to be a circle centered at the corner. The circle expands bigger and bigger, going across the whole sub-Brillouin zone (the red large circle), then it becomes a circle centered at the origin, and finally it disappears after decaying as a singular point at the origin. After such a $\mathbb{Z}_2$ nontrivial small nodal circle is created at the corner of the sub-Brillouin zone, the topological number of any one-dimensional subsystem parametrized by k_z inside the small circle is increased by 1, while any one outside has

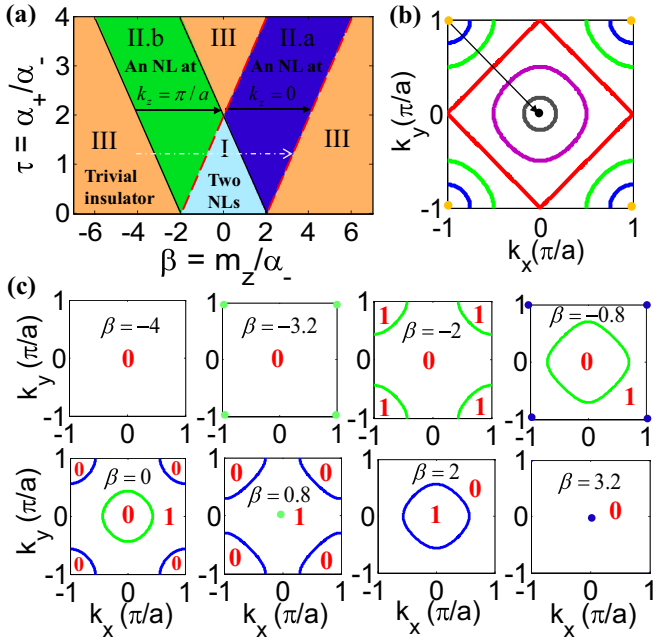

FIG. 4. Phase diagram and tunable NL states. (a) Phase diagram. III, II.a, II.b, and I correspond to a trivial insulator, an NL on the $k_z = 0$ plane, an NL on the $k_z = \pi/a$ plane, and two coexisting NLs on the two planes, respectively. (b) The evolution of an NL during the increase of β is denoted by the black arrows in (a). (c) The distribution of the topological numbers of one-dimensional subsystems on the k_x-k_y plane in difference phases during the increase of β is marked by the white arrow in (a).

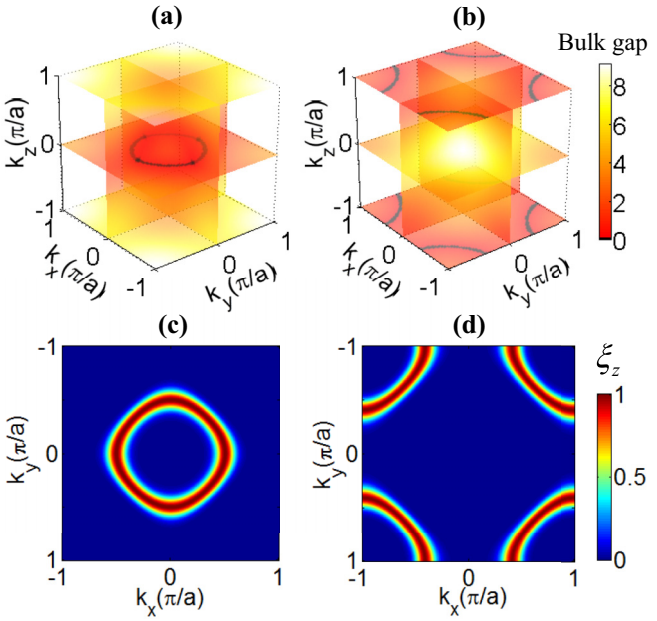

FIG. 5. The bulk gap with the gap-closing points forming a nodal ring and its detection. (a) A nodal ring on the $k_z = 0$ plane with the parameter $m_z = 2.0$. (b) A nodal ring on the $k_z = \pi/a$ plane with the parameter $m_z = -1.8$. (c,d) The momentum distribution of the atomic transfer fraction $\xi_z(k_x,k_y)$ with the parameter $F = 0.2$. The maximum positions form a curve that reveals the nodal ring in (a) and (b), respectively. Other parameters in (a)–(d) are $t_\uparrow = 1$ as the energy unit, $t_\downarrow = t_{so} = 0.3$.

its topological number unchanged, which can be seen from the model discussed in Fig. 2 considering the fact that the creation of the circle results in only continuous deformations for the outside ones. Having this in mind, we can infer the topological number of any one-dimensional system with fixed in-plane momentum $\mathbf{k}_\parallel \equiv (k_x,k_y)$ in any region of the phase diagram. For instance, the distribution of topological number γ in the k_x-k_y plane along the white arrow in Fig. 4(a) is shown in Fig. 4(c), which has also been confirmed by the numerical simulation. It is noted that in the fifth subfigure with $\beta = 0$, the ones at the corner of the sub-Brillouin zone have the topological number $\gamma = 1 + 1 \equiv 0 \mod 2$. In addition, the shape of the NL can changes from a circle to a square, as shown in Fig. 4(b), due to the fact that the k_η^2 terms in the continuum Hamiltonian (9) are replaced by the $\cos(k_\eta a)$ terms in this lattice system with Hamiltonian (21). Thus, in the proposed optical lattice system, one can realize tunable NL states by simply varying the ratio parameter β via the laser fields.

In the following, we focus on the single NL cases and further study the properties of the NL state. In Figs. 5(a) and 5(b), we plot the bulk energy gap $E_+(\mathbf{k}) - E_-(\mathbf{k})$ for typical parameters, which clearly show the gap-closing points forming the NLs on the $k_z = 0$ and $k_z = \pi/a$ planes, respectively. On the two planes, the upper and lower energy surfaces touch along a ring with a constant energy ε_a in phase II.a and ε_b in phase II.b. The constant energies $\varepsilon_a = -\alpha_+(\alpha_+ - m_z)/\alpha_- - \alpha_-$ and $\varepsilon_b = -\alpha_+(\alpha_+ + m_z)/\alpha_- + \alpha_-$ come from the $f_0(\mathbf{k})\sigma_0$ term in Hamiltonian (21), respectively. This term breaks the chiral symmetry but only shifts the nodal ring from zero energy without modifying its shape. Actually, it does not affect the topological stability of the NLs, but it gives the surface states a dispersion [3,21]. In phase II.a, the low-energy effective Hamiltonian near $\mathbf{K_r} = (0,0,0)$ is given by

$$\mathcal{H}_{\text{eff}}(\mathbf{q}) = \left[b_1\left(q_x^2 + q_y^2\right) + b_0 q_z^2 - \lambda_1\right]\sigma_3 - v_z q_z \sigma_2 + \left[b_0\left(q_x^2 + q_y^2\right) + b_1 q_z^2 - \lambda_0\right]\sigma_0, \tag{25}$$

where $\mathbf{q} = \mathbf{k} - \mathbf{K_r}$, $b_0 = a^2\alpha_+/2$, $b_1 = a^2\alpha_-/2$, $\lambda_1 = 2\alpha_- + \alpha_+ - m_z$, $v_z = 2at_{so}$, and $\lambda_0 = 2\alpha_+ + \alpha_-$. In phase II.b, the low-energy effective Hamiltonian near $\mathbf{K}'_\mathbf{r} = (\pi/a,\pi/a,\pi/a)$ is $\mathcal{H}'_{\text{eff}}(\mathbf{q}) = -\mathcal{H}_{\text{eff}}(\mathbf{q})$ with redefined $\mathbf{q} = \mathbf{k} - \mathbf{K}'_\mathbf{r}$ in this case. The effective Hamiltonian (25) takes the form of the two-band model (9), and it captures the essential features of the nodal ring states on the $q_z = 0$ plane of radius $\sqrt{\lambda_1/b_1}$ when its size is small (see Fig. 4).

At this stage, we elaborate on the fact that the NLs can be detected using the Bloch-Zener-oscillation method, which has been experimentally demonstrated to probe the Dirac points in a honeycomb optical lattice [65,66]. A basic idea lies in the fact that the band-touching points can be monitored from the atomic fraction tunneling to the excited band in Bloch oscillations. We can use noninteracting fermionic atoms or an incoherent distribution of bosonic atoms with the population being homogeneous in the momentum space initially prepared in the lower band [42]. A constant force F is applied along the z axis and pushes the atoms moving along the k_z direction.

After a Bloch cycle, we can obtain the momentum distribution of the transfer fraction to the upper band from time-of-flight imaging [65,66]. In this case, the transfer fraction $\xi_z(\mathbf{k}_\parallel)$ is given by

$$\xi_z(\mathbf{k}_\parallel) = P_{\mathrm{LZ}}(\mathbf{k}_\parallel) = e^{-\pi\Delta_z^2(\mathbf{k}_\parallel)/4v_zF}, \tag{26}$$

where P_{LZ} is the Landau-Zener transition probability and $\Delta_z = (E_+ - E_-)|_{k_z=0,\pi/a}$ denotes the energy gap for the transition along the k_z direction. Figures 5(c) and 5(d) show the typical momentum distribution $\xi_z(\mathbf{k}_\parallel)$, where each point of maximum transfer in the k_x-k_y plane corresponds to a nodal point, and all the points form an NL, corresponding to the cases in Figs. 5(a) and 5(b), respectively. The peaks in $\xi_z(\mathbf{k}_\parallel)$ are sharp as the transition probability in a Landau-Zener event increases exponentially as the energy gap decreases, such that the momentum distribution of the atomic transfer fraction with its maximum positions can well reveal the shape of an NL.

IV. TOPOLOGICAL PROPERTIES OF THE SIMULATED NODAL LOOP STATES

In this section, we proceed to investigate the topological properties of the simulated NL states and present practical methods for their experimental detection in this cold-atom system. We first show the quantized Berry phase characterizing the NL states in the bulk and then consider the related nontrivial surface states.

A. Quantized Berry phase: $\mathbb{Z}_2$ topological invariant

As analyzed in the preceding section, Hamiltonian (21) preserves the combined $\mathcal{PT}$ symmetry. This guarantees the symmetry-protected topological stability of the $\mathcal{PT}$-invariant NLs in the three-dimensional Brillouin zone and a quantized Berry phase γ in units of π that characterizes its topological protection, even in the presence of $\mathcal{P}$ and $\mathcal{T}$ breaking perturbation $\mathcal{H}_P$. If a closed loop in the momentum space is pierced by the NL, one has $\gamma = 1$ (i.e., π Berry phase), otherwise $\gamma = 0$, which represents a $\mathbb{Z}_2$-type invariant. The same invariant can be written if the loop is chosen parallel to k_z, i.e., with fixed $\mathbf{k}_\parallel$, since it is closed at $k_z = \pm\pi/a$ due to periodic boundary conditions. Thus the topological invariant of the NL states may be evaluated as

$$\gamma(\mathbf{k}_\parallel) = -\frac{i}{\pi}\sum_{E_n<E_{\mathrm{F}}}\int_{-\pi/a}^{\pi/a}\langle u_n(\mathbf{k})|\partial_{k_z}|u_n(\mathbf{k})\rangle dk_z, \tag{27}$$

where the sum is over the filled Bloch eigenstates $|u_n(\mathbf{k})\rangle$ of Hamiltonian (21) with the Fermi energy E_F. Equation (27) indicates that the topological properties of the system can be parameterized by $\mathbf{k}_\parallel$ as the nontrivial Zak phase for an effective gapped one-dimensional system. Using the Bloch Hamiltonian (21) with given $\mathbf{k}_\parallel$, we verify that $\gamma = 1$ for $\mathbf{k}_\parallel$ inside the projected NL while $\gamma = 0$ outside, as shown in Fig. 6(a).

For fermionic atoms in this optical lattice, one can directly probe $\gamma(\mathbf{k}_\parallel)$ by measuring the Bloch wave function $c_{n\sigma}(\mathbf{k})$ from $|u_n(\mathbf{k})\rangle = c_{n\uparrow}(\mathbf{k})\,|\uparrow\rangle + c_{n\downarrow}(\mathbf{k})\,|\downarrow\rangle$ with time-of-flight imaging [67]. One first maps out the atomic momentum distribution $\rho_{n\sigma}(\mathbf{k}) = |c_{n\sigma}(\mathbf{k})|^2$ for the filled band using the conventional time-of-flight imaging. One then may measure

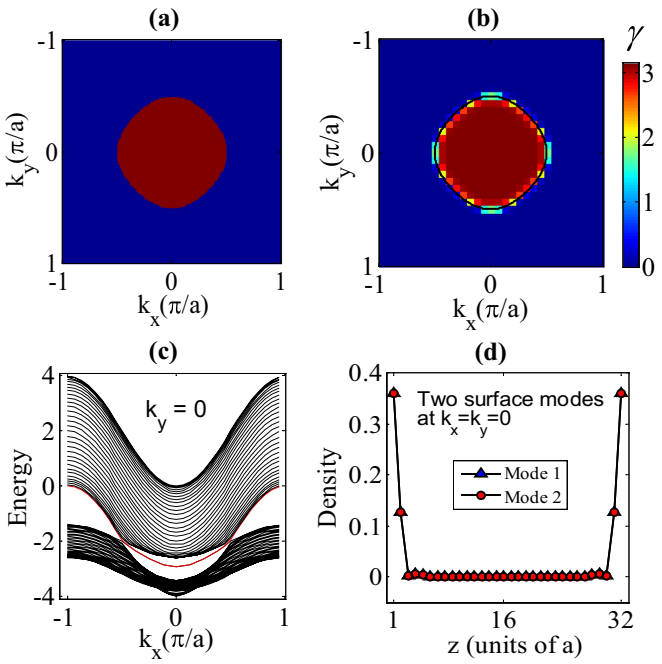

FIG. 6. (a) The Berry phase $\gamma(k_x,k_y)$ calculated by using the Bloch Hamiltonian (21). (b) The simulated measurement of Berry phase $\gamma(k_x,k_y)$ with the lattice size $32 \times 32 \times 32$ and an additional harmonic trap with the parameter $\nu = 0.001$ (see the text) by using Eq. (28). The black solid line denotes the nodal loop in this case. (c) The energy spectrum with respect to k_x for fixed $k_y = 0$ and open boundary condition along the z axis, and the surface states inside the gap. (d) The density distribution of two surface modes at $k_x = k_y = 0$. Other parameters in (a)–(d) are $t_\uparrow = 1$ as the energy unit, $t_\downarrow = t_{\mathrm{so}} = 0.3$, and $m_z = 2.0$.

the phase information of $c_{n\sigma}(\mathbf{k})$ by introducing a $\pi/2$ rotation between the two spin states with an impulsive pulse light before the flight of atoms, which induces the transition $c_{n\uparrow}(\mathbf{k}) \to [c_{n\uparrow}(\mathbf{k}) + c_{n\downarrow}(\mathbf{k})]/\sqrt{2}$ and $c_{n\downarrow}(\mathbf{k}) \to [c_{n\uparrow}(\mathbf{k}) - c_{n\downarrow}(\mathbf{k})]/\sqrt{2}$. With this pulse, the difference between $|c_\uparrow(\mathbf{k}) \pm c_\downarrow(\mathbf{k})|^2/2$ measured through time-of-flight imaging gives the real part of the interference terms $\mathrm{Re}[c^*_{n\uparrow}(\mathbf{k})c_{n\downarrow}(\mathbf{k})]$. The imaginary part $\mathrm{Im}[c^*_{n\uparrow}(\mathbf{k})c_{n\downarrow}(\mathbf{k})]$ can be obtained by the same way with a different rotation. The measurement of the population and interference terms determines the Bloch wave function up to an arbitrary overall phase $c_{n\sigma}(\mathbf{k}) \to c_{n\sigma}(\mathbf{k})e^{i\chi(\mathbf{k})}$, where $\chi(\mathbf{k})$ in general depends on $\mathbf{k}$ instead of the spin index. The arbitrary $\mathbf{k}$-dependent phase poses an obstacle to measure the topological invariant [67]. To overcome this difficulty, we use a gauge-invariant method to calculate the Berry phase [68],

$$\gamma(\mathbf{k}_\parallel) = \frac{1}{\pi}\sum_{j=0}^{N_j-1}\mathrm{Arg}[\det\langle u_n(\mathbf{k}_\parallel,k_j^z)|u_{n'}(\mathbf{k}_\parallel,k_{j+1}^z)\rangle], \tag{28}$$

where k_z in the BZ is discretized into small N_j intervals with $k_j^z = -\pi/a + 2j\pi/N_j a$, the overlap phase $\arg[\bullet] = \mathrm{imag}\{\ln[\bullet]\}$, and the determinant is that of a matrix formed by allowing n and n' to run over filled Bloch eigenstates.

To demonstrate that the method is feasible in a realistic experiment, we numerically simulate the proposed detection of the Berry phase $\gamma(\mathbf{k}_\parallel)$ with a finite lattice system and an

additional harmonic trap,

$$\hat{H}_{\text{trap}} = \frac{1}{2} m_a \omega^2 \sum_{\mathbf{i},\sigma} d_{\mathbf{i}}^2 \hat{a}_{\mathbf{i},\sigma}^{\dagger} \hat{a}_{\mathbf{i},\sigma}, \tag{29}$$

where ω is the trap frequency and $d_{\mathbf{i}}$ is the distance from the center of the trap to the lattice site $\mathbf{i}$. We can use $\nu = m_a \omega^2 a^2 / 2t_{\uparrow}$ to parametrize the influence of this trapping potential. For a typical experiment with $a \approx 400$ nm and $t_{\uparrow} \approx 1$ kHz, μ is on the order of 10^{-3} for ^{6}Li or ^{40}Ka atoms in a trap with $\omega \approx 2\pi \times 50$ Hz. In numerical simulations, we perform the spin rotation and obtain the momentum distribution under a different spin basis by diagonalizing the real-space Hamiltonian on a finite lattice and using a Fourier transformation [67]. The numerical result of $\gamma(\mathbf{k}_{\parallel})$ for a finite lattice $32 \times 32 \times 32$ with a weak harmonic trap ($\nu = 0.001$) and typical parameters is shown in Fig. 6(b). Compared with the result shown in Fig. 6(a), in this case the $\mathbf{k}_{\parallel}$ regime with $\gamma = 1$ slightly shrinks from that of the ideal NL [black solid line in Fig. 6(b)] and the sharp boundary between $\gamma = 0$ and 1 becomes relatively smooth, both of which are due to the trapping potential and the finite-size effects.

B. Protected surface states

According to the bulk-edge correspondence, the topological NL state with the Berry phase $\gamma(\mathbf{k}_{\parallel})$ is related to edge states at the end of the one-dimensional system with a fixed $\mathbf{k}_{\parallel}$ [21,68,69]. Hence, for a fixed $\mathbf{k}_{\parallel}$ and two surfaces (upper and lower surfaces) along the z axis, two in-gap states appear at the surface Brillouin zone when $\gamma(\mathbf{k}_{\parallel}) \neq 0$. This indicates that surface states appear for all $\gamma(\mathbf{k}_{\parallel})$ inside the area enclosed by the projected NL on the surface plane. With the $f_0(\mathbf{k})\sigma_0$ term, the surface states acquire a dispersion proportional to $f_0(k_x, k_y, 0)$. In Fig. 6(c), we plot the energy spectrum with respect to k_x for fixed $k_y = 0$ and an open boundary condition along the z axis (with 32 lattice sites), which shows the surface states inside the gap denoted by red solid lines connecting the two band-touching points. The density distribution of the two corresponding surface modes at $k_x = k_y = 0$ is shown in Fig. 6(d). The surface states for other k_y are similar, and they merge into the bulk bands when the system become a trivial insulator. For this system in phase II.a, the surface modes perpendicular to the z direction with fixed $\mathbf{k}_{\parallel}$ can be described by the effective Hamiltonian $H_z(\mathbf{k}_{\parallel}) = i v_z \sigma_2 \partial_z + g_z(\mathbf{k}_{\parallel})\sigma_3 + g_0(\mathbf{k}_{\parallel})\sigma_0$ up to linear order in $k_z \to -i\partial_z$, where $g_z(\mathbf{k}_{\parallel}) = m_z - \alpha_+ - \alpha_-[\cos(k_x a) + \cos(k_y a)]$ and $g_0(\mathbf{k}_{\parallel}) = -\alpha_- - \alpha_+[\cos(k_x a) + \cos(k_y a)]$.

In the optical lattice, the surface states may be washed out by the smooth harmonic potential and become indistinguishable from the bulk states. To circumvent this problem, one can use a steep confining potential or cut the atomic hopping along the z axis by locally tuning the effective Rabi frequency of the Raman lasers. Under this condition, the protected surface states can be probed through Bragg spectroscopy [53,70,71]. One could shine another two laser beams at a certain angle to induce a specifically tuned Raman transition from an occupied spin state to an unoccupied hyperfine level and focus them near the surface of the three-dimensional atomic cloud [71]. When the momentum and energy conservation conditions are satisfied, the atomic transition rate is peaked and can be measured. By scanning the Raman frequency difference, the surface energy-momentum dispersion relation can be mapped out from these Bragg signals [70,71].

V. CONCLUSION

In summary, we have presented a topological classification of NLs in systems with $\mathcal{PT}$ symmetry. In three-dimensional momentum space, only $\mathcal{PT}$-invariant NLs are topologically protected with a $\mathbb{Z}_2$ classification. Motivated by this observation, we have proposed a realistic experimental scheme to realize $\mathcal{PT}$-invariant topological NL states with cold atoms in a three-dimensional optical lattice, which have tunable loop-shaped Fermi lines with twofold degeneracy in the bulk spectrum and nontrivial surface states. The NL states are actually protected by the combined $\mathcal{PT}$ symmetry even in the absence of both $\mathcal{P}$ and $\mathcal{T}$ symmetries, and they are characterized by a quantized Berry phase (a $\mathbb{Z}_2$-type invariant). We have also shown that (i) the characteristic NLs can be detected by measuring the atomic transfer fractions in a Bloch-Zener oscillation, (ii) the topological charge can be measured based on the time-of-flight imaging, and (iii) the surface states can be probed through Bragg spectroscopy. The experimental realization and detection of $\mathcal{PT}$-symmetry protected NL states in cold-atom systems will be regarded as an important advance in the field of quantum simulation, paving the way for exploring exotic $\mathcal{PT}$-invariant topological physics.

ACKNOWLEDGMENTS

We thank M. Gong for useful discussions. This work was supported by the NSFC (Grant No. 11474153), the PCSIRT (Grant No. IRT1243), the SKPBR of China (Grant No. 2013CB921804), the SRFYTSCNU (Grant No. 15KJ16), the FDYT (Grant No. 2015KQNCX023), and the RGC of Hong Kong (HKU173051/14P and HKU173055/15P).

[1] M. Z. Hasan and C. L. Kane, Colloquium: Topological insulators, Rev. Mod. Phys. **82**, 3045 (2010).
[2] X.-L. Qi and S. C. Zhang, Topological insulators and superconductors, Rev. Mod. Phys. **83**, 1057 (2011).
[3] G. E. Volovik, *The Universe in a Helium Droplet* (Clarendon, Oxford, 2003).
[4] A. P. Schnyder, S. Ryu, A. Furusaki, and A. W. W. Ludwig, Classification of topological insulators and superconductors in three spatial dimensions, Phys. Rev. B **78**, 195125 (2008).
[5] S. Ryu, A. P. Schnyder, A. Furusaki, and A. W. Ludwig, Topological insulators and superconductors: Tenfold way and dimensional hierarchy, New J. Phys. **12**, 065010 (2010).

[6] Y. X. Zhao and Z. D. Wang, Topological Classification and Stability of Fermi Surfaces, Phys. Rev. Lett. **110**, 240404 (2013); Topological connection between the stability of Fermi surfaces and topological insulators and superconductors, Phys. Rev. B **89**, 075111 (2014); Disordered Weyl Semimetals and their Topological Family, Phys. Rev. Lett. **114**, 206602 (2015).

[7] A. Kitaev, Periodic table for topological insulators and superconductors, AIP Conf. Proc. **1134**, 22 (2009).

[8] T. Morimoto and A. Furusaki, Topological classification with additional symmetries from Clifford algebras, Phys. Rev. B **88**, 125129 (2013).

[9] B.-J. Yang and N. Nagaosa, Classification of stable three-dimensional Dirac semimetals with nontrivial topology, Nat. Commun. **5**, 4898 (2014); B.-J. Yang, T. Morimoto, and N. Nagaosa, Topological charges of three-dimensional Dirac semimetals with rotation symmetry, Phys. Rev. B **92**, 165120 (2015).

[10] C.-K. Chiu and A. P. Schnyder, Classification of reflection-symmetry-protected topological semimetals and nodal superconductors, Phys. Rev. B **90**, 205136 (2014).

[11] C.-K. Chiu, J. C. Y. Teo, A. P. Schnyder, and S. Ryu, Classification of topological quantum matter with symmetries, arXiv:1505.03535.

[12] Y. X. Zhao and Z. D. Wang, Novel $\mathbb{Z}_2$ Topological Metals and Semimetals, Phys. Rev. Lett. **116**, 016401 (2016).

[13] J. Dalibard, F. Gerbier, G. Juzeliūnas, and P. Öhberg, Colloquium: Artificial gauge potentials for neutral atoms, Rev. Mod. Phys. **83**, 1523 (2011).

[14] N. Goldman, G. Juzeliūnas, P. Öhberg, and I. B. Spielman, Light-induced gauge fields for ultracold atoms, Rep. Prog. Phys. **77**, 126401 (2014).

[15] V. Galitski and I. B. Spielman, Spin-orbit coupling in quantum gases, Nature (London) **494**, 49 (2013); H. Zhai, Degenerate quantum gases with spin-orbit coupling: A review, Rep. Prog. Phys. **78**, 026001 (2015).

[16] L. Lu, J. D. Joannopoul, and M. Soljačíc, Topological photonics, Nat. Photon. **8**, 821 (2014).

[17] Z. Wang, Y. Sun, X.-Q. Chen, C. Franchini, G. Xu, H. Weng, X. Dai, and Z. Fang, Dirac semimetal and topological phase transitions in A_3Bi (A = Na,K,Rb), Phys. Rev. B **85**, 195320 (2012); Z. Wang, H. Weng, Q. Wu, X. Dai, and Z. Fang, Three-dimensional Dirac semimetal and quantum transport in Cd_3As_2, *ibid.* **88**, 125427 (2013).

[18] X. Wan, A. M. Turner, A. Vishwanath, and S. Y. Savrasov, Topological semimetal and Fermi-arc surface states in the electronic structure of pyrochlore iridates, Phys. Rev. B **83**, 205101 (2011).

[19] L. Balents, Viewpoint: Weyl electrons kiss, Physics **4**, 36 (2011).

[20] G. Xu, H. Weng, Z. Wang, X. Dai, and Z. Fang, Chern Semimetal and the Quantized Anomalous Hall Effect in $HgCr_2Se_4$, Phys. Rev. Lett. **107**, 186806 (2011).

[21] A. A. Burkov, M. D. Hook, and L. Balents, Topological nodal semimetals, Phys. Rev. B **84**, 235126 (2011).

[22] C. Fang, Y. Chen, H.-Y. Kee, and L. Fu, Topological nodal line semimetals with and without spin-orbital coupling, Phys. Rev. B **92**, 081201(R) (2015).

[23] S.-Y. Xu, I. Belopolski, N. Alidoust, M. Neupane, C. Zhang, R. Sankar, S.-M. Huang, C.-C. Lee, G. Chang, B. Wang, G. Bian, H. Zheng, D. S. Sanchez, F. Chou, H. Lin, S. Jia, and M. Z. Hasan, Discovery of a Weyl fermion semimetal and topological Fermi arcs, Science **349**, 613 (2015).

[24] B. Q. Lv, H. M. Weng, B. B. Fu, X. P. Wang, H. Miao, J. Ma, P. Richard, X. C. Huang, L. X. Zhao, G. F. Chen, Z. Fang, X. Dai, T. Qian, and H. Ding, Experimental Discovery of Weyl Semimetal TaAs, Phys. Rev. X **5**, 031013 (2015).

[25] Z. K. Liu, J. Jiang, B. Zhou, Z. J. Wang, Y. Zhang, H. M. Weng, D. Prabhakaran, S-K. Mo, H. Peng, P. Dudin, T. Kim, M. Hoesch, Z. Fang, X. Dai, Z. X. Shen, D. L. Feng, Z. Hussain, and Y. L. Chen, A stable three-dimensional topological Dirac semimetal Cd_3As_2, Nat. Mater. **13**, 677 (2014).

[26] Z. K. Liu, B. Zhou, Z. J. Wang, H. M. Weng, D. Prabhakaran, S.-K. Mo, Y. Zhang, Z. X. Shen, Z. Fang, X. Dai, Z. Hussain, and Y. L. Chen, Discovery of a three-dimensional topological Dirac semimetal, Na_3Bi, Science **343**, 864 (2014).

[27] M. Neupane, S.-Y. Xu, R. Sankar, N. Alidoust, G. Bian, C. Liu, I. Belopolski, T.-R. Chang, H.-T. Jeng, H. Lin, A. Bansil, F. Chou, and M. Z. Hasan, Observation of a three-dimensional topological Dirac semimetal phase in high-mobility Cd_3As_2, Nat. Commun. **5**, 3786 (2014).

[28] S.-Y. Xu, C. Liu, S. K. Kushwaha, R. Sankar, J. W. Krizan, I. Belopolski, M. Neupane, G. Bian, N. Alidoust, T.-R. Chang, H.-T. Jeng, C.-Y. Huang, W.-F. Tsai, H. Lin, P. P. Shibayev, F.-C. Chou, R. J. Cava, and M. Zahid Hasan, Observation of Fermi arc surface states in a topological metal, Science **347**, 294 (2015).

[29] L. Lu, L. Fu, J. D. Joannopoulos, and M. Soljačíc, Weyl points and line nodes in gyroid photonic crystals, Nat. Photon. **7**, 294 (2013).

[30] L. Lu, Z. Wang, D. Ye, L. Ran, L. Fu, J. D. Joannopoulos, and M. Soljačíc, Experimental observation of Weyl points, Science **349**, 622 (2015).

[31] M. Xiao, W.-J. Chen, W.-Y. He, and C. T. Chan, Synthetic gauge flux and Weyl points in acoustic systems, Nat. Phys. **11**, 920 (2015).

[32] H. Weng, Y. Liang, Q. Xu, R. Yu, Z. Fang, X. Dai, and Y. Kawazoe, Topological node-line semimetal in three-dimensional graphene networks, Phys. Rev. B **92**, 045108 (2015).

[33] K. Mullen, B. Uchoa, and D. T. Glatzhofer, Line of Dirac Nodes in Hyperhoneycomb Lattices, Phys. Rev. Lett. **115**, 026403 (2015).

[34] Y. Kim, B. J. Wieder, C. L. Kane, and A. M. Rappe, Dirac Line Nodes in Inversion-Symmetric Crystals, Phys. Rev. Lett. **115**, 036806 (2015).

[35] R. Yu, H. Weng, Z. Fang, X. Dai, and X. Hu, Topological Node-Line Semimetal and Dirac Semimetal State in Antiperovskite Cu_3PdN, Phys. Rev. Lett. **115**, 036807 (2015).

[36] G. Bian, T.-R. Chang, R. Sankar, S.-Y. Xu, H. Zheng, T. Neupert, C.-K. Chiu, S.-M. Huang, G. Chang, I. Belopolski, D. S. Sanchez, M. Neupane, N. Alidoust, C. Liu, B. Wang, C.-C. Lee, H.-T. Jeng, C. Zhang, Z. Yuan, S. Jia, A. Bansil, F. Chou, H. Lin, and M. Zahid Hasan, Topological nodal-line fermions in the non-centrosymmetric superconductor compound $PbTaSe_2$, Nat. Commun. **7**, 10556 (2016).

[37] Y.-H. Chan, C.-K. Chiu, M. Y. Chou, and A. P. Schnyder, Topological semi-metals with line nodes and drumhead surface states, arXiv:1510.02759.

[38] M. Lewenstein, A. Sanpera, V. Ahufinger, B. Damski, A. S. De, and U. Sen, Ultracold atomic gases in optical lattices:

Mimicking condensed matter physics and beyond, Adv. Phys. **56**, 243 (2007).

[39] M. Atala, M. Aidelsburger, J. T. Barreiro, D. Abanin, T. Kitagawa, E. Demler, and I. Bloch, Direct measurement of the Zak phase in topological Bloch bands, Nat. Phys. **9**, 795 (2013).

[40] H. Miyake, G. A. Siviloglou, C. J. Kennedy, W. C. Burton, and W. Ketterle, Realizing the Harper Hamiltonian with Laser-Assisted Tunneling in Optical Lattices, Phys. Rev. Lett. **111**, 185302 (2013).

[41] M. Aidelsburger, M. Atala, M. Lohse, J. T. Barreiro, B. Paredes, and I. Bloch, Realization of the Hofstadter Hamiltonian with Ultracold Atoms in Optical Lattices, Phys. Rev. Lett. **111**, 185301 (2013).

[42] M. Aidelsburger, M. Lohse, C. Schweizer, M. Atala, J. T. Barreiro, S. Nascimbène, N. R. Cooper, I. Bloch, and N. Goldman, Measuring the Chern number of Hofstadter bands with ultracold bosonic atoms, Nat. Phys. **11**, 162 (2015).

[43] G. Jotzu, M. Messer, R. Desbuquois, M. Lebrat, T. Uehlinger, D. Greif, and T. Esslinger, Experimental realisation of the topological Haldane model with ultracold fermions, Nature (London) **515**, 237 (2014).

[44] L. Duca, T. Li, M. Reitter, I. Bloch, M. Schleier-Smith, and U. Schneider, An Aharonov-Bohm interferometer for determining Bloch band topology, Science **347**, 288 (2015).

[45] M. Mancini, G. Pagano, G. Cappellini, L. Livi, M. Rider, J. Catani, C. Sias, P. Zoller, M. Inguscio, M. Dalmonte, and L. Fallani, Observation of chiral edge states with neutral fermions in synthetic Hall ribbons, Science **349**, 1510 (2015).

[46] B. K. Stuhl, H.-I. Lu, L. M. Aycock, D. Genkina, and I. B. Spielman, Visualizing edge states with an atomic Bose gas in the quantum Hall regime, Science **349**, 1514 (2015).

[47] D. R. Hofstadter, Energy levels and wave functions of Bloch electrons in rational and irrational magnetic fields, Phys. Rev. B **14**, 2239 (1976); P. G. Harper, The general motion of conduction electrons in a uniform magnetic field, with application to the diamagnetism of metals, Proc. Phys. Soc. London, Sect. A **68**, 874 (1955).

[48] F. D. M. Haldane, Model for a Quantum Hall Effect without Landau Levels: Condensed-Matter Realization of the "Parity Anomaly," Phys. Rev. Lett. **61**, 2015 (1988).

[49] N. Goldman, I. Satija, P. Nikolic, A. Bermudez, M. A. Martin-Delgado, M. Lewenstein, and I. B. Spielman, Realistic Time-Reversal Invariant Topological Insulators with Neutral Atoms, Phys. Rev. Lett. **105**, 255302 (2010).

[50] B. Béri and N. R. Copper, Z_2 Topological Insulators in Ultracold Atomic Gases, Phys. Rev. Lett. **107**, 145301 (2011).

[51] X.-J. Liu, Z.-X. Liu, and M. Cheng, Manipulating Topological Edge Spins in a One-Dimensional Optical Lattice, Phys. Rev. Lett. **110**, 076401 (2013).

[52] X.-J. Liu, K. T. Law, and T. K. Ng, Realization of 2D Spin-Orbit Interaction and Exotic Topological Orders in Cold Atoms, Phys. Rev. Lett. **112**, 086401 (2014).

[53] S.-T. Wang, D.-L. Deng, and L.-M. Duan, Probe of Three-Dimensional Chiral Topological Insulators in an Optical Lattice, Phys. Rev. Lett. **113**, 033002 (2014).

[54] T. Dubcek, C. J. Kennedy, L. Lu, W. Ketterle, M. Soljacic, and H. Buljan, Weyl Points in Three-Dimensional Optical Lattices: Synthetic Magnetic Monopoles in Momentum Space, Phys. Rev. Lett. **114**, 225301 (2015).

[55] W.-Y. He, S. Zhang, and K. T. Law, The realization and dectection of Weyl semimetals in cold atomic systems, arXiv:1501.02348.

[56] D.-W. Zhang, S. L. Zhu, and Z. D. Wang, Simulating and exploring Weyl semimetal physics with cold atoms in a two-dimensional optical lattice, Phys. Rev. A **92**, 013632 (2015).

[57] S. Ganeshan and S. Das Sarma, Constructing a Weyl semimetal by stacking one-dimensional topological phases, Phys. Rev. B **91**, 125438 (2015).

[58] K. Sun, W. V. Liu, A. Hemmerich, and S. Das Sarma, Topological semimetal in a fermionic optical lattice, Nat. Phys. **8**, 67 (2012).

[59] J. H. Jiang, Tunable topological Weyl semimetal from simple-cubic lattices with staggered fluxes, Phys. Rev. A **85**, 033640 (2012).

[60] M. Karoubi, *K-Theory. An Introduction* (Springer, New York, 1978).

[61] M. F. Atiyah, R. Bott, and A. Shapiro, Clifford modules, Topology **3**, 3 (1964).

[62] We highlight below the relevant and key results for the classification of $\mathcal{PT}$ symmetry relevant to our systems, while we refer readers to Y. X. Zhao, A. P. Schnyder, and Z. D. Wang, Unified Theory of $\mathcal{PT}$- and $\mathcal{CP}$ Invariant Topological Metals and Nodal Superconductors, Phys. Rev. Lett. **116**, 156402 (2016).

[63] D. Jaksch, C. Bruder, J. I. Cirac, C. W. Gardiner, and P. Zoller, Cold Bosonic Atoms in Optical Lattices, Phys. Rev. Lett. **81**, 3108 (1998).

[64] Y. Xu and C. Zhang, Dirac and Weyl rings in three dimensional cold atom optical lattices, arXiv:1510.03355.

[65] L. Tarruell, D. Greif, T. Uehlinger, G. Jotzu, and T. Esslinger, Creating, moving and merging Dirac points with a Fermi gas in a tunable honeycomb lattice, Nature (London) **483**, 302 (2012); T. Uehlinger, D. Greif, G. Jotzu, L. Tarruell, T. Esslinger, L. Wang, and M. Troyer, Double transfer through Dirac points in a tunable honeycomb optical lattice, Eur. Phys. J. Spec. Top. **217**, 121 (2013).

[66] L.-K. Lim, J.-N. Fuchs, and G. Montambaux, Bloch-Zener Oscillations Across a Merging Transition of Dirac Points, Phys. Rev. Lett. **108**, 175303 (2012).

[67] D.-L. Deng, S.-T. Wang, and L.-M. Duan, Direct probe of topological order for cold atoms, Phys. Rev. A **90**, 041601(R) (2014).

[68] R. D. King-Smith and D. Vanderbilt, Theory of polarization of crystalline solids, Phys. Rev. B **47**, 1651 (1993); R. Resta, Macroscopic polarization in crystalline dielectrics: The geometric phase approach, Rev. Mod. Phys. **66**, 899 (1994).

[69] R. Jackiw and C. Rebbi, Solitons with fermion number 1/2, Phys. Rev. D **13**, 3398 (1976).

[70] S.-L. Zhu, B. Wang, and L.-M. Duan, Simulation and Detection of Dirac Fermions with Cold Atoms in an Optical Lattice, Phys. Rev. Lett. **98**, 260402 (2007).

[71] N. Goldman, J. Beugnon, and F. Gerbier, Detecting Chiral Edge States in the Hofstadter Optical Lattice, Phys. Rev. Lett. **108**, 255303 (2012).